



Self-assembled CoFeNi alloy-based perovskite oxide as the catalyst layer for stable direct ammonia protonic ceramic fuel cells

Tianjiu Zhu^a, Desheng Feng^b, Zhixin Luo^c, Zehua Wang^c, Beibei Ma^a, Zongping Shao^{c,*}, Zhonghua Zhu^{a,**}, Lei Ge^{d,e,***}

^a School of Chemical Engineering, The University of Queensland, Brisbane, 4072, Australia

^b Department of Chemical Engineering, The University of Melbourne, Melbourne, 3010, Australia

^c WA School of Mines: Minerals, Energy & Chemical Engineering (WASM-MECE), Curtin University, Perth, 6102, Australia

^d Centre for Future Materials, University of Southern Queensland, Springfield, 4300, Australia

^e School of Engineering, University of Southern Queensland, Springfield, QLD, 4300, Australia

ARTICLE INFO

Handling Editor: Fanglin F. Chen

Keywords:

Direct ammonia fuel cells
Protonic ceramic fuel cells
Anode catalytic layer
Self-assembled perovskite oxides
Ammonia decomposition reaction
In situ alloy formation

ABSTRACT

Ammonia is a promising fuel for protonic ceramic fuel cells (PCFCs) as it has a higher energy density and storage capacity than hydrogen. However, due to low catalytic activity and poor stability, the conventional Ni and proton conductor cermet anode struggles to operate efficiently in ammonia atmospheres at intermediate temperatures such as 550 °C. In this study, we present a self-assembled BaCo_{0.43}Fe_{0.43}Ni_{0.17}O_{3-δ}/BaCe_{0.8}Y_{0.2}O_{3-δ} (BMO7/BCY3) as an anode catalytic layer (ACL), in situ phase separation and reduction of BaO/CoFeNi from BMO phase and nano alloy grown on the proton conductor phase (BCY) host oxide under reduced atmosphere. The co-reduction of the Co, Fe, and Ni promotes Fe reduction, and the resulting alloy aids in ammonia adsorption and nitrogen desorption, leading to high ammonia decomposition rates at reduced temperatures (550 °C). Consequently, PCFC with the BMO7/BCY3 ACL demonstrates enhanced power output with a 74 % improvement and more importantly a significantly improved cell lifetime with 60 h operation without obvious power degradation compared to the gradual deterioration of the cell without an ACL that completely failed at 43h when using ammonia fuel at 550 °C.

1. Introduction

Protonic ceramic fuel cells (PCFC) are effective power generation devices that can convert chemical energy from several fuel sources, such as hydrogen (H₂) and ammonia (NH₃), to electricity at intermediate temperature ranges between 400 and 600 °C [1–5]. Compared to last-generation solid oxide fuel cells (SOFCs), PCFCs offer lower activation energy for proton conduction, improved thermal cycling stability, and enhanced fuel flexibility, making them promising candidates for next-generation energy conversion systems. While hydrogen remains the primary focus in PCFC research, its low volumetric energy density (~8 MJ/L at 700 bar) and challenging storage requirements, such as cryogenic liquefaction (–253 °C) or high-pressure compression, limit its commercial viability [6–8]. As an alternative, NH₃ has a higher volumetric energy density (~12.7 MJ/L), can be liquefied at –33 °C under

atmospheric pressure, and benefits from an established transportation infrastructure [9,10]. These advantages make ammonia a viable fuel candidate for PCFCs. However, its direct utilization in PCFCs faces challenges, including high-temperature decomposition requirements, and electrode degradation due to metal nitride formation, necessitating further material and catalytic optimizations.

However, the application of ammonia in PCFCs is limited by several challenges. A key limitation is the low ammonia conversion rate at intermediate temperatures, which restricts hydrogen availability for electrochemical oxidation, thereby reducing power output. Ammonia decomposition is an endothermic reaction that requires high operating temperatures (>600 °C) for efficient conversion. At lower temperatures, the reaction becomes sluggish due to kinetic constraints in N–H bond dissociation and N₂ recombination, leading to partial decomposition and unreacted NH₃ crossover, which further degrades cell performance. In

* Corresponding author.

** Corresponding author.

*** Corresponding author. Centre for Future Materials, University of Southern Queensland, Springfield, 4300, Australia.

E-mail addresses: zongping.shao@curtin.edu.au (Z. Shao), z.zhu@uq.edu.au (Z. Zhu), lei.ge@unisq.edu.au (L. Ge).

<https://doi.org/10.1016/j.ijhydene.2025.04.461>

Received 24 March 2025; Received in revised form 23 April 2025; Accepted 26 April 2025

Available online 30 April 2025

0360-3199/© 2025 The Authors. Published by Elsevier Ltd on behalf of Hydrogen Energy Publications LLC. This is an open access article under the CC BY license (<http://creativecommons.org/licenses/by/4.0/>).

conventional PCFCs, the anode is typically a Ni-BZCYYb ($\text{BaZr}_{0.1}\text{Ce}_{0.7}\text{Y}_{0.1}\text{Yb}_{0.1}\text{O}_{3-\delta}$) cermet, which provides both protonic and electronic conduction while enabling catalytic activity for hydrogen oxidation [11–14]. When ammonia is used as fuel in PCFCs, the NH_3 is first decomposed into nitrogen and hydrogen, the hydrogen then being further oxidised at the anode [15,16]. However, the ammonia decomposition reaction is sluggish at reduced temperatures. Feng reported that the ammonia conversion rate for Ni + BZCYYb could reach 95 % at 600 °C but decrease to 46 % at 500 °C [17]. This reduction limits the application of ammonia in PCFCs at lower temperature ranges. In addition to power output, microstructural changes in the anode material also shorten the lifespan of the PCFCs. During the ammonia dehydrogenation process, Ni_3N forms on the Ni surface [18,19]. However, the Ni_3N is not thermally stable in either ammonia or hydrogen atmospheres at intermediate temperatures, and it decomposes back into metallic Ni [20]. This decomposition process causes Ni particle agglomeration, disrupts electronic percolation and weakens the mechanical integrity of the anode, ultimately leading to performance degradation and failure of the PCFC [21,22]. Therefore, mitigating ammonia-induced degradation while ensuring efficient NH_3 conversion remains a critical challenge in the development of ammonia-fueled PCFCs.

To improve the lifetime of the PCFCs when operating with ammonia, applying efficient catalysts for ammonia pre-cracking is an effective solution [23]. However, the complexity of the PCFC system makes catalyst integration challenging. One option is to use a separate ammonia cracking reactor before the PCFCs. This external reactor ensures that the PCFC does not come into direct contact with ammonia, helping to protect the Ni from poisoning [24]. However, this approach increases system complexity, cost, and heat management challenges, making it less viable for commercial applications. An alternative strategy is the integration of a reforming layer directly on the PCFC anode, enabling in situ ammonia decomposition while simplifying the system architecture and reducing additional infrastructure costs.

Noble metals such as Ru and Pd, as well as non-noble metals like Ni and Fe, are commonly used as catalysts for ammonia decomposition, as the reaction occurs on the metal surface [25–29]. Noble metals generally offer better ammonia decomposition efficiency compared to transition metals [23,28,30]. However, incorporating noble metals such as Pd and Ru into the anode significantly increases the cost, which is a limitation for the development of the Direct Ammonia Solid Oxide Fuel Cell (DASOFC) system. As a more cost-effective alternative, transition metal catalysts like Fe and Co have been used in PCFCs, achieving satisfactory ammonia conversion rates at temperatures above 650 °C [31–33]. However, the ammonia decomposition efficiency of single transition metal catalysts at lower temperatures limits their use [19].

To address these challenges, alloying metal catalysts offers a solution. The formation of alloy catalysts can improve the performance of both noble and non-noble metal catalysts and reduce the amount of precious metals required [34,35]. For example, Liu et al. introduced Ru and Fe into the anode supporting layer, forming an in-situ RuFe alloy that enhances ammonia decomposition. This approach mitigates the poisoning of Ni at the anode and improves the stability of the PCFC at 600 °C under ammonia exposure [36]. However, the cost and exsolution efficiency of noble metal catalysts limits their widespread use. Transition metal alloys also perform better than single-metal catalysts in ammonia decomposition reactions. For example, a NiCo alloy catalyst supported by $\text{La}_{0.52}\text{Sr}_{0.28}\text{TiO}_3$ outperforms single Ni or Co catalysts on the same support at 800 °C [37]. However, these alloys still face challenges in achieving satisfactory ammonia decomposition efficiency at reduced temperatures below 550 °C.

To maximize catalytic activity, controlling the size and dispersion of metal particles is crucial. Smaller particles provide a larger active surface area for the ammonia decomposition reaction, while high dispersion reduces metal loading and enhances metal-oxide interactions. Techniques such as in situ exsolution and infiltration are used to load metal particles onto support materials in a way that achieves small, well-

dispersed nanoparticles [35,38,39]. Compared to conventional infiltration, exsolution of metal nanoparticles from perovskite oxides offers smaller particle sizes, better distribution, greater stability, and better metal-support interaction [40,41]. Therefore, perovskite oxide catalysts could exsolve metal nanoparticles in reducing atmospheres are promising for ammonia decomposition reactions.

In addition to metal selection, the choice of support material plays a critical role in ammonia decomposition. The right support can optimize the performance of the metal catalyst. For example, proton-conducting materials as supports for the same metal can yield higher ammonia conversion rates compared to conventional supports [42]. In the case of DASOFC anode supports, using proton-conducting $\text{BaZr}_{0.8}\text{Y}_{0.2}\text{O}_{3-\delta}$ instead of oxygen-conducting materials like YSZ or SDC boosts the ammonia decomposition activity of Ni, even at the same catalyst loading [43,44]. Herein, to solve the issues mentioned above, a catalyst made of transition metal alloy deposited by a proton conductive substrate with a high ammonia decomposition efficiency is desired.

In this study, we applied an anode catalytic layer (ACL) strategy for PCFCs, using a highly dispersed non-noble metal alloy catalyst on a proton-conducting support. This is achieved by the in-situ formation of a transition metal alloy catalyst from a self-assembled perovskite oxide, $\text{BaCo}_{0.43}\text{Fe}_{0.43}\text{Ni}_{0.17}\text{O}_{3-\delta}/\text{BaCe}_{0.8}\text{Y}_{0.2}\text{O}_{3-\delta}$ (BMO7/BCY3) with a molar ratio of 7:3. The highly dispersed nano-size CoFeNi (CFN) alloy particles form from one of the self-assembled phases under reducing conditions at high temperatures, while another proton-conducting phase improves ammonia decomposition performance. This combination helps maintain the stability of the PCFCs in ammonia environments. Compared to single metal phase separation samples from $\text{BaCoO}_{3-\delta}/\text{BaCe}_{0.8}\text{Y}_{0.2}\text{O}_{3-\delta}$ (BCO7/BCY3), $\text{BaFeO}_{3-\delta}/\text{BaCe}_{0.8}\text{Y}_{0.2}\text{O}_{3-\delta}$ (BFO7/BCY3), and $\text{BaNiO}_{3-\delta}/\text{BaCe}_{0.8}\text{Y}_{0.2}\text{O}_{3-\delta}$ (BNO7/BCY3), the alloy particles formed from reduced BMO7/BCY3 (r-BMO7/BCY3) exhibit superior ammonia decomposition performance due to enhanced exsolution efficiency, improved ammonia adsorption, and better nitrogen desorption kinetics. As a result, the r-BMO7/BCY3 ACL efficiently decomposes ammonia and protects the Ni microstructure at the PCFC anode from ammonia poisoning. This leads to improved stability of the PCFC single cell at reduced temperatures, such as 550 °C, compared to cells without an ACL, which experience significant performance degradation.

2. Methodology

2.1. Material synthesis

The BMOx/BCY10-x series catalyst materials, the PCFC electrolyte material $\text{BaZr}_{0.1}\text{Ce}_{0.7}\text{Y}_{0.1}\text{Yb}_{0.1}\text{O}_{3-\delta}$ (BZCYYb), and PCFC cathode material $\text{BaCo}_{0.4}\text{Fe}_{0.4}\text{Zr}_{0.1}\text{Y}_{0.1}\text{O}_{3-\delta}$ (BCFZY) were synthesised by using the sol-gel method. Taking $\text{BaCo}_{0.43}\text{Fe}_{0.43}\text{Ni}_{0.17}\text{O}_{3-\delta}/\text{BaCe}_{0.8}\text{Y}_{0.2}\text{O}_{3-\delta}$ (BMO7/BCY3) as an example, stoichiometric amounts of $\text{Ba}(\text{NO}_3)_2$, $\text{Co}(\text{NO}_3)_2 \cdot 6\text{H}_2\text{O}$, $\text{Fe}(\text{NO}_3)_3 \cdot 9\text{H}_2\text{O}$, $\text{Ni}(\text{NO}_3)_2$, $\text{Ce}(\text{NO}_3)_3 \cdot 6\text{H}_2\text{O}$ and $\text{Y}(\text{NO}_3)_3 \cdot 6\text{H}_2\text{O}$ were dissolved in DI water. Citric acid (CA) was added to the solution, followed by the addition of ethylenediaminetetraacetic acid (EDTA) in the ammonia solution. The metal: CA: EDTA molar ratio was maintained at 1: 2: 1. The pH of the solution was adjusted to ~10 using ammonia solution. The gel was formed after the water evaporated under 80 °C, the gel was then put into an oven at 260 °C for 5h to get the precursor powder. The precursor powder was then sintered at 1000 °C for 5h to obtain the final perovskite oxide phase.

2.2. Fabrication of single cells

The PCFC anode was prepared by mixing nickel oxide, BZCYYb, and starch with a mass ratio of 6:4:1. The electrolyte powder was made by mixing 1 wt% NiO to the BZCYYb powder. A 0.4g amount of anode powder was first pressed under a lower pressure, followed by the coating of 0.02 g of electrolyte powder onto the anode disk surface. The two layers were then co-pressed under higher pressure and sintered at

1450 °C for 5 h to obtain the PCFC half-cells. The cathode slurry was made by ball milling 1 g BCFZY cathode powder with 10 mL isopropanol, 1 mL glycerol, and 2 mL ethylene glycol for 30 min. The anode reforming layer slurry (ammonia decomposition catalyst) was prepared using the same method. The BCFZY was applied onto the electrolyte side of the half-cell via spray coating with an active area of 0.45 cm², and the cell was finally sintered at 1000 °C for 2 h to obtain the full single cell.

2.3. Ammonia decomposition activity test

For the ammonia decomposition activity test, 0.2 g of catalyst powder, sieved through a 100 μm sieve, was placed in a continuous fixed-bed quartz reactor inside a vertical furnace. The catalyst was heated to 600 °C in a hydrogen flow at a rate of 30 mL min⁻¹, with a heating rate of 10 °C min⁻¹. It was then held at 600 °C for 1 h to reduce the catalyst. Afterward, the gas flow was switched to ammonia at a rate of 20 mL min⁻¹, and the catalyst was heated within a temperature range of 400–600 °C, with intervals of 50 °C. After 1 h of stabilization, the gas product was collected from the reactor outlet and analysed using a Shimadzu GC-2014 gas chromatograph equipped with a thermal conductivity detector (TCD).

2.4. Electrochemical performance measurement

The silver paste was brushed onto the cathode side of the single cell with a configuration of the NiO + BZCYYb/BZCYYb/BCFZY. Silver wires were used to connect the electrode surface to the electrochemical test station. The single cell was then mounted onto the ceramic tube and sealed using a ceramic bond (Aremco 671).

The single cell was first heated to 600 °C with a heating rate of 5 °C min⁻¹. Once it reached 600 °C, H₂ (50 mL min⁻¹) was supplied to the anode and air was supplied to the cathode side. The single-cell output was characterized using linear scanning voltammetry (LSV) and electrochemical impedance spectroscopy (EIS) tests, conducted with an Autolab PGSTAT302 N potentiostat. The testing temperature ranges between 600 and 400 °C. Subsequently, ammonia was supplied to the anode side at a flow rate of 20 mL min⁻¹, replacing hydrogen. The cell was discharged at 0.2 A cm⁻² at 550 °C for long-term stability testing of the ammonia-fueled PCFC.

2.5. Characterization

The crystal structure and composition analysis of the as-synthesised and reduced catalysts was conducted by X-ray diffraction (XRD). Lab XRD was performed by a Bruker D8 Advance diffractometer at the Centre for Microscopy and Microanalysis (CMM), which equipped with a Bragg-Brentano geometry and a Cu X-ray source. Synchrotron X-ray diffraction (SXR) was conducted in the Australian Synchrotron powder diffraction beamline at the Australian Nuclear Science and Technology Organisation (ANSTO). For reduced catalyst samples, the samples were treated in H₂ at 600 °C for 5 h. For SXR measurements of the reduced catalyst samples, the powder was quenched after hydrogen treatment, then loaded into quartz capillaries with a diameter of 0.4 mm, and sealed with wax prior to the measurement. Lab XRD and SXR data were analysed using the GSAS-II software [45]. The instrument parameters were determined using standard reference materials 640c and 660b from the National Institute of Standards and Technology for Lab XRD and SXR, respectively [46,47]. For the refinement of BMO7/BCY3, the crystallographic model was initially based on BaCoO₃ and BaCe_{0.9}Y_{0.1}O₃. For the refinement of r-BMO7/BCY3 using the SXR results, BaCe_{0.9}Y_{0.1}O₃, BaCO₃, and Fe_{0.33}Co_{0.48}Ni_{0.19} were used as the starting crystallographic models [48]. The morphology of the catalysts and cells was examined by using field emission scanning electron microscopy (FE-SEM, JEOL JSM-7800F) at CMM. High-resolution transmission electron microscopy (HR-TEM, Hitachi HF 5000, Japan) was employed to inspect the interface between phases and CFN alloy

nanoparticles in the r-BMO7/BCY3 sample. To study the valence state of the transition metal in different catalyst samples, X-ray photoelectron spectroscopy (XPS) was conducted using a Kratos Axis Supra Plus XPS at CMM. The collected XPS data were analysed using the CasaXPS software [49], and the carbon peak at 284.4 eV was used for calibration. Nitrogen adsorption-desorption isotherms were measured at 77K using a Micromeritics TriStar II surface area analyser to assess the surface area of the catalyst samples. Prior to nitrogen adsorption, the samples were heated in a vacuum at 200 °C for 12 h using a Micromeritics VacPrep 061 sample preparation device. The surface areas of the samples were determined using a Brunauer-Emmett-Teller (BET) model.

To further investigate metal particle phase separation status and properties, ammonia adsorption, and nitrogen adsorption process, hydrogen temperature-programmed reduction (TPR), ammonia temperature-programmed desorption (TPD) and nitrogen TPD were performed. These tests were conducted using a BELCAT (BEL Japan) system equipped with a TCD. To measure the TPR profiles, samples were heated to 500 °C and held for 1 h before being cooled to room temperature in a flowing He atmosphere (20 mL min⁻¹) to remove adsorbed water or other species. The samples were then exposed to H₂ at a flow rate of 20 mL min⁻¹ and heated to 900 °C, while the H₂-TPR profile was recorded. For NH₃ TPD test, samples were exposed to NH₃ at 20 mL min⁻¹ at 50 °C for 1 h, then heated in He gas while the NH₃ TPD profile was recorded. For the N₂ TPD test, samples were exposed to N₂ at 20 mL min⁻¹ at 600 °C for 1 h, then cooled to room temperature under N₂ atmosphere. He was then used to heat the samples while the N₂ TPD profile was recorded.

3. Result and discussion

3.1. Structure and morphology of catalysts

Fig. 1a illustrates a schematic of the in-situ formation process of the CFN nanoalloy catalyst on the surface of BaCe_{0.9}Y_{0.1}O_{2.95} (BCY). Upon synthesis, the BMO7/BCY3 self-assembles into two phases: one phase is similar to BCY, while the other phase (BMO) resembles BaCoO₃ (BCO). When exposed to a reduced atmosphere at high temperatures, such as 600 °C, CFN metal alloy nanoparticles come from both BMO and BCY phase, and BaO comes out from the BMO phase. As a result, the remaining BMO phase reduces in size, and BaO and nanoparticles are highly dispersed across both the remaining BMO and BCY phases. During the ammonia decomposition reaction, the CFN on the BaO and BCY support will efficiently convert ammonia into hydrogen and nitrogen.

Fig. 1b shows the XRD patterns of as-synthesised BMO7/BCY3, BCY (PDF#01-083-5709) and BCO (PDF#04-019-7747) with PDF card numbers 04-019-7747 and 01-083-5709 [48] at top; r-BMO7/BCY3, BCY, BaCO₃ (PDF#00-045-1471), and Fe_{0.33}Co_{0.48}Ni_{0.19} (PDF#04-016-6385). As observed in Fig. 1b, the as-synthesis BMO7/BCY3 sample has a phase separation into an orthorhombic and a cubic phase. Similar self-assembly composite structures have been reported by several researchers [50–53]. Based on the Rietveld refinement of BMO7/BCY3, as shown in Fig. S1 and Table S1, phase separation is observed in BMO7/BCY3. The as-synthesised BMO7/BCY3 contains two crystalline phases: a major cubic phase (72.6 wt%) with a space group of *Pm-3m*, similar to perovskite BCO, which has a lattice parameter of *a* = *b* = *c* = 4.1 Å, and a minor orthorhombic phase (27.4 wt%) with a space group of *Pnma*, similar to perovskite oxide BCY, which has a lattice parameter of *a* = 6.2077 Å, *b* = 8.8020 Å, and *c* = 6.2138 Å. While the BCY phase matched well with the peak positions and intensities from the reference pattern, the BCO phase exhibited lattice expansion, resulting in a shift of all peaks to lower angles, which might be due to the dopant of the Fe and Ni. Fig. 1c and Table S2 show the Rietveld refinement result for r-BMO7/BCY3 from Synchrotron XRD (SXR), where two orthorhombic and one cubic crystalline phases are observed. The first phase is a CFN alloy phase (24.5 wt%), with lattice parameters *a* = 3.5357 Å, the second phases (71.5 wt%) is similar to

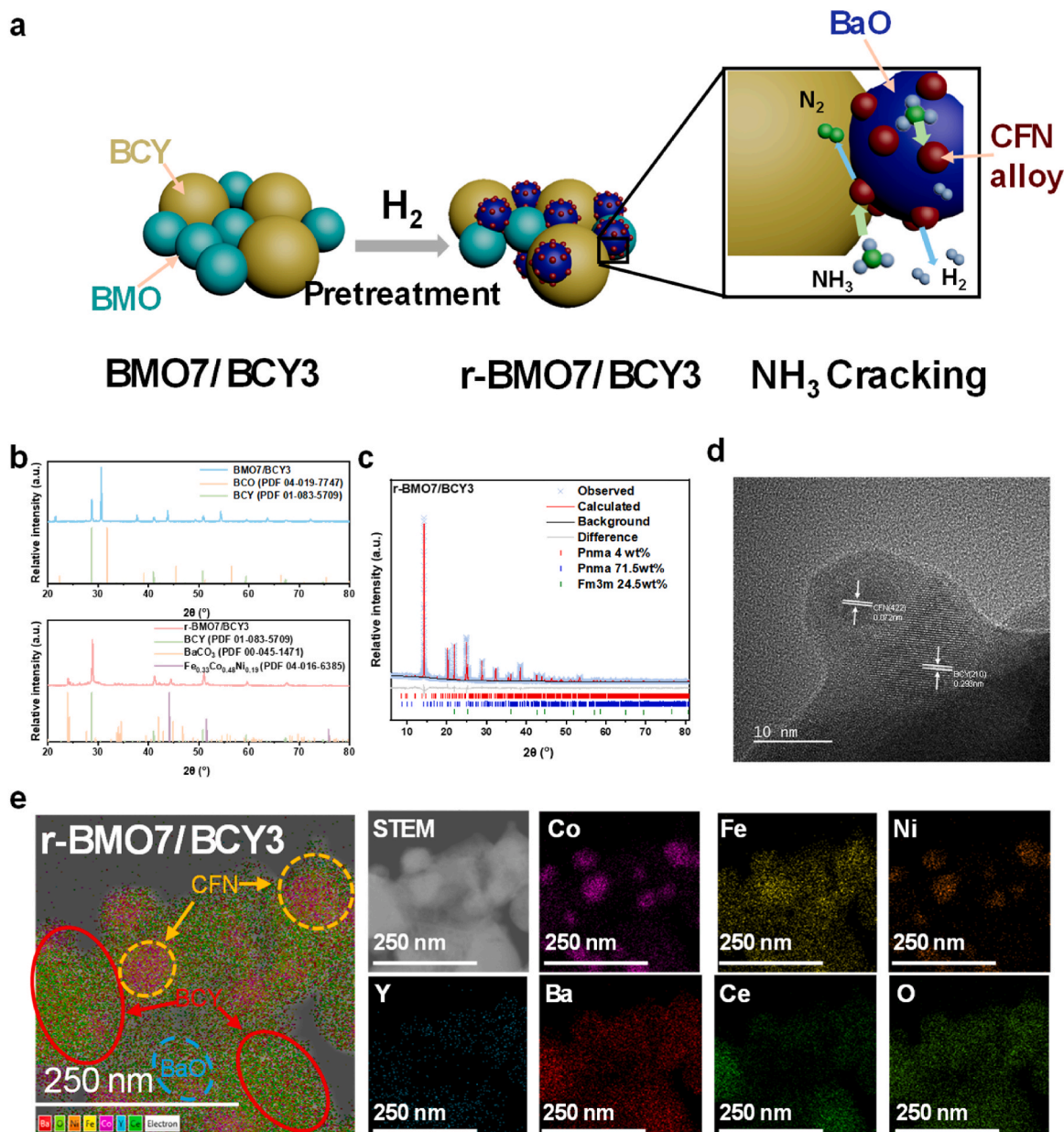


Fig. 1. (a) Schematic of the formation of the CFN nanoalloy from BMO7/BCY3, and operation in ammonia condition, (b) XRD patterns of (top) BMO7/BCY3, BCY, and BCO, and (bottom) r-BMO7/BCY3, BCY, BaCO₃, and Fe_{0.33}Co_{0.48}Ni_{0.19}, (c) Rietveld refinement profile using SXRD data of r-BMO7/BCY3, (d) The HR-TEM image and (e) STEM-EDX mapping results for r-BMO7/BCY3.

BCY, with lattice parameters $a = 6.2146 \text{ \AA}$, $b = 8.7751 \text{ \AA}$, and $c = 6.2336 \text{ \AA}$, and the third phases (4 wt%) is similar to BaCO₃, with a lattice parameter of $a = 6.4144 \text{ \AA}$, $b = 5.3203 \text{ \AA}$, and $c = 8.8722 \text{ \AA}$. The formation of BaCO₃ is observed in both the lab-based XRD and SXRD results, as shown in Fig. 1b and c. This may be attributed to contamination from ambient CO₂ during sample transfer and characterization. The SEM and XRD results presented in Fig. S2 demonstrate the effect of air exposure over time (2h and 24 h) on the r-BMO7/BCY3 samples. Similar heterogeneous phase separation can be also found in different nanoparticle exsolution research [54–56]. Catalyst BCO7/BCY3, BFO7/BCY3 and BNO7/BCY3 with varying single metal concentrations of Co, Fe, and Ni in the B-site were also synthesised using the sol-gel method as reference sample for comparison. The XRD patterns for these samples are presented in Figure S3 a, b, c. From Fig. S3, a single orthorhombic crystal structure is observed in the samples with lower transition metal loading, while a second cubic phase forms as the metal content increases

in the perovskite oxide, hexagonal phase also forms as the metal concentration increases to 70 % [50,57].

The morphology of the alloy or metal particles was observed by scanning electron microscopy (SEM). The SEM images of the as-synthesised BMO7/BCY3, BCO7/BCY3, BFO7/BCY3, and BNO7/BCY3 samples show the presence of nanoparticles on the surface of the bars, which result from phase separation (Fig. S4). The SEM images of the reduced samples are shown in Fig. S5, r-BMO7/BCY3 and r-BFO7/BCY3 were covered by nanoparticles. In addition to nanoparticles, surface reconstruction is observed in r-BMO7/BCY3, r-BCO7/BCY3, and r-BNO7/BCY3 due to vigorous phase separation and reduction reactions.

Transmission electron microscopy (TEM) was also performed to confirm the formation and morphology of the CFN alloy. The high-resolution TEM (HR-TEM) results of the r-BMO7/BCY3, shown in Fig. 1d, reveal the CFN nanoalloys with a lattice spacing of 0.07 nm (CFN (422) diffraction plane) were socketed into the BCY phase with a

lattice spacing of 0.29 nm which corresponding to BCY (210) diffraction plane. The STEM image of the r-BMO7/BCY3, shown in Fig. 1e, confirms the formation of nanoparticles on the support material surface. The morphology, particle size, and composition of the nanoparticles were confirmed by energy-dispersive X-ray (EDX) mapping, as shown in Fig. 1e. The Co, Fe, and Ni round nanoalloys, with a diameter of 50 nm, were confirmed based on the distribution of the Co, Fe, and Ni elements. The BCY, BaO, and CFN alloy are highlighted on Fig. 1e, for the BCY segregated area, the stronger signal of Ba, Ce, Y, and O can be observed; for the BaO-rich area, the Ba and O obtained a higher intensity while Ce, Y, Co, Fe, and Ni have relatively lower intensity; for the CFN area, the Co, Fe, and Ni signals are high on the area that Ba, Ce and Y also strong. The Ba, Ce, and O distribution confirms that the nanoalloy particles are deposited and well in contact with the BCY. Moreover, no Ba-rich regions were observed, suggesting that BaO is evenly distributed onto both BCY and BMO surfaces.

3.2. Evaluation of ammonia decomposition catalytic activity

To investigate the phase separation and metal reduction behaviours of the transition metals in the BCY system, hydrogen temperature programmed reduction (H_2 -TPR) analysis was performed on BMO7/BCY3, BFO7/BCY3, BNO7/BCY3, and BCO7/BCY3. Fig. 2a shows the H_2 -TPR result between 100 and 900 °C. All samples exhibit the first reduction step starting around 300 °C, likely related to the reduction of metal ions in the B-site. As the metal in the B-site was reduced, more oxygen vacancies are generated, facilitating the following reduction process at higher temperatures [58]. The temperatures at which hydrogen consumption occurred during the second reduction step (above 500 °C) varied. The reduction of Fe from $Fe^{4+}/Fe^{3+}/Fe^{2+}$ to Fe^0 mainly occurred at 697 °C, the reduction of Co from Co^{3+}/Co^{2+} to Co^0 took place after 586 °C, and Ni^{2+} reduction was observed around 631 °C. However, for BMO7/BCY3, the first reduction step around 600 °C, suggesting that the reduction process for BMO7/BCY3 was more vigorous than for the single metal dopants in the BCY system. The second reduction step

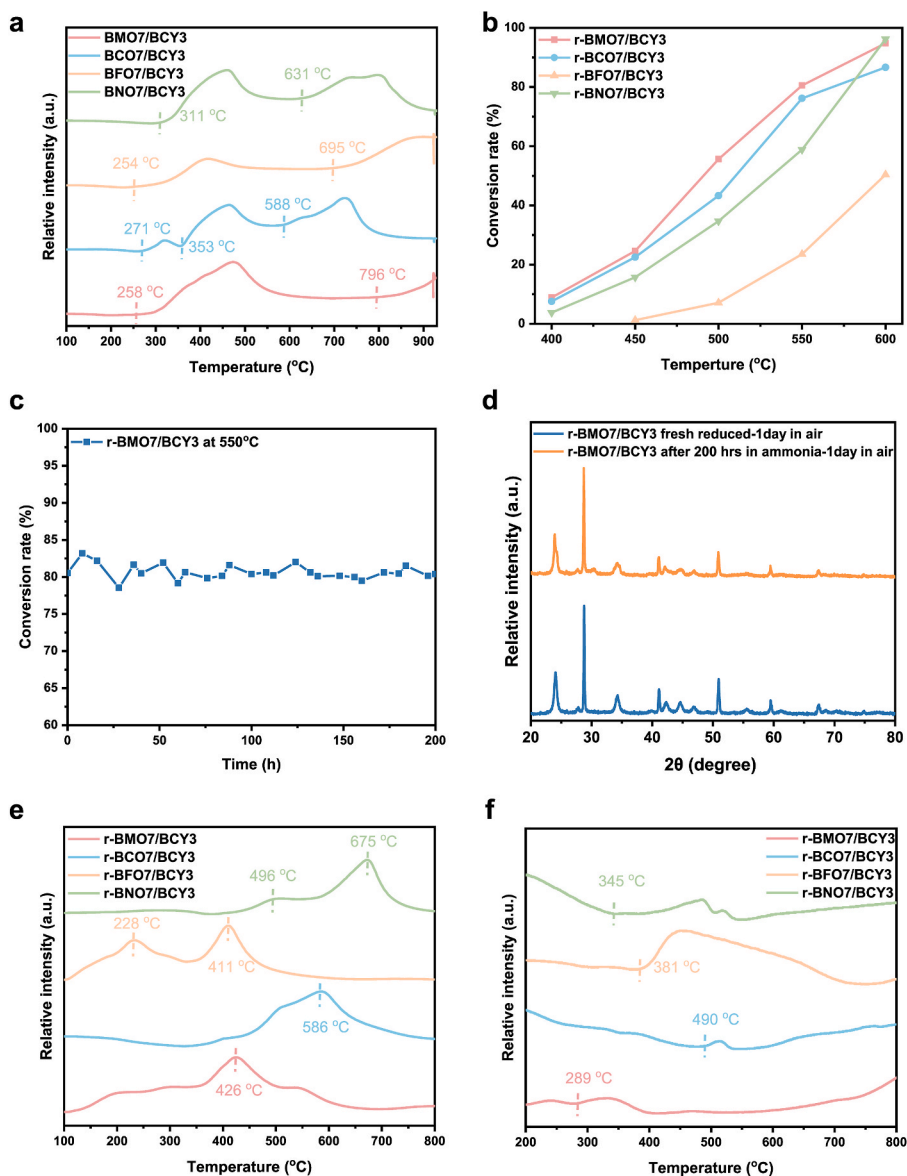


Fig. 2. (a) H_2 TPR profile of four catalysts between 100 and 900 °C, (b) Ammonia conversion rate of four catalysts between 400 and 600 °C, (c) Ammonia conversion rate of r-BMO7/BCY3 catalyst in fix bed reactor at 550 °C for 200hrs, (d) XRD patterns of r-BMO7/BCY3 catalyst freshly reduced in hydrogen at 600 °C for 1hr, and tested in fix bed reactor at 550 °C for 200hrs (24h exposed to air before XRD), (e) NH_3 TPD profile of four catalysts between 100 and 800 °C. (f) N_2 TPD profile of four catalysts between 200 and 800 °C.

for BMO7/BCY3 began at 796 °C, indicating that the system became more stable after the initial reduction compared to other single-metal samples. For the catalyst operating below 600 °C, a second reduction or reconstruction will not occur during the operating temperatures, offering a more stable structure in operating conditions. The co-doping of the transition metals into the B-site of the perovskite oxide facilitates the reduction of metals from the metal oxide to metal particles and moves from the perovskite structure to the surface at a lower reduction temperature.

To examine the metal reduction status and valence states of the metals on the perovskite oxide surface, X-ray photoelectron spectroscopy (XPS) was employed. As illustrated in Figure S6 a, b, c, after 1h of reduction at 600 °C, Co, Fe, and Ni metal particles were observed on r-BMO7/BCY3 compared to the freshly synthesised samples [59]. In r-BMO7/BCY3, 5 % of Co, 4 % of Fe, and 8 % of Ni were reduced as alloy metal particles from the main cubic phase, whereas only 3 % of Co, 2 % of Fe, and 3 % of Ni were observed in r-BCO7/BCY3, r-BFO7/BCY3, and r-BNO7/BCY3 respectively (Figure S6 d, e, f). For Ni or Co with lower exsolution Gibbs free energy [60,61], only minor differences in metal concentration were observed due to the easier metal reduction process [62]. The significantly higher Fe phase separation in r-BMO7/BCY3 compared to r-BFO7/BCY3 suggests that the formation of metal alloy nanoparticles is more efficient in the alloy system than in the single metal reduction. By combining the H₂-TPR and XPS data from the single metal and alloy phase separation samples, it can be concluded that the alloy co-reduction process leads to increased loading of the highly dispersed CFN alloy.

Fig. 2b compares the ammonia decomposition catalytic activity of r-BMO7/BCY3 with that of r-BCO7/BCY3, r-BFO7/BCY3, and r-BNO7/BCY3, between 600 and 400 °C. The ammonia conversion rates of r-BMO7/BCY3 at 600, 550, 500, 450, and 400 °C are 94.80 %, 80.54 %, 55.64 %, 24.60 % and 8.89 %, respectively, which are higher than those observed for all other single-metal-doped samples. The CFN alloy nanoparticles are active catalysts for converting the ammonia into hydrogen and nitrogen. In addition to CFN alloy, the BCY support offers a proton conduction condition that facilitates the ammonia decomposition reaction [44]. Furthermore, the BaO from BMO phases could also improve the ammonia decomposition process as the basicity of the material is increased [63]. The surface area of the catalyst samples was confirmed by using N₂ adsorption-desorption, which can be found in Table S3 and Fig. S7, ruling out surface area differences as a factor contributing to the observed variations in ammonia decomposition performance.

Based on the TPR result, the first reduction finishes at around 600 °C. Fig. S8 shows the change in the ammonia conversion rate of the synthesised BMO7/BCY3 at 600 °C over time. After 15 min, an 81 % ammonia decomposition rate is achieved. The hydrogen produced from ammonia decomposition reduces BMO7/BCY3, leading to the formation of nanoalloys on the surface, which further enhances the ammonia decomposition reaction. A stable ammonia conversion rate is reached after 60 min. The ammonia conversion rate of r-BMO7/BCY3 at 550 °C with different gas space velocities is shown in Fig. S9. At a space velocity of 6000 ml g_{cat}⁻¹ h⁻¹, the conversion rate is 80.54 %, which slightly decreases at higher space velocities, such as 12000 ml g_{cat}⁻¹ h⁻¹, where the conversion rate drops to 74 %.

In contrast, the ammonia decomposition performance of single-metal-doped catalysts with varying metal concentrations is given in Fig. S10. These data demonstrate that the optimal ammonia conversion performance occurs at 30 % Co, 30 % Fe, and 10 % Ni concentrations. Beyond this threshold, increasing the metal concentration does not improve ammonia conversion performance. Based on this, BMO7/BCY3 was selected as the metal alloy material for further testing and analysis.

Fig. 2c presents the stability test results for r-BMO7/BCY3 in ammonia for 200h at 550 °C. The ammonia conversion rate of the sample after 200h in ammonia remains at a similar level to the freshly reduced sample, indicating stable ammonia conversion performance

over the extended operation. Fig. 2d shows the XRD patterns of r-BMO7/BCY3 samples before and after the 200-h ammonia stability test (exposed in air for 24h). The primary phases in BMO7/BCY3 remain unchanged after the 200-h ammonia decomposition reaction.

During the ammonia decomposition reaction on the metal surface, ammonia is first adsorbed, followed by a dehydrogenation reaction where hydrogen is removed from the ammonia molecules, and nitrogen desorbs from the metal surface [64]. To understand this process on the metal of the catalysts, N₂ and NH₃ TPD were conducted to measure the ammonia absorption and nitrogen desorption abilities for metal alloy catalysts and single metal catalysts.

Fig. 2e shows the NH₃ TPD result. Combined with the ammonia decomposition data, under 400 °C, the lower desorption temperature from desorption peaks means a weaker interaction between ammonia and catalysts, while at higher temperatures, the desorption peaks might indicate a strong interaction between the gas and the catalysts [65]. The metal alloy catalyst, r-BMO7/BCY3, exhibits a peak at 426 °C, which is higher than that of the catalyst with Fe loading, suggesting a better ammonia adsorption ability compared to r-BFO7/BCY3. Single-metal catalysts with Ni or Co, show a higher desorption temperature than r-BMO7/BCY3, indicating a weaker interaction between the metal alloy catalyst and ammonia gas after introducing Fe into the system. However, the r-BMO7/BCY3 has a larger peak area than the single metal catalyst r-BNO7/BCY3 and r-BCO7/BCY3, which indicates a better ammonia capacity of the r-BMO7/BCY3.

The N₂-TPD result can be found in Fig. 2f, a similar trend for the N₂ desorption on the Ni/Fe catalysts has been reported [66,67]. Compared to single-metal samples, the N₂ desorption temperature of the r-BMO7/BCY3 is much lower at 289 °C, which shows an improved N₂ desorption ability. This helps the N₂ desorption after the ammonia decomposition reaction, which promotes the ammonia conversion reaction efficiency.

3.3. PCFC single cell performance

To assess the suitability of r-BMO7/BCY3 as an ACL for the PCFCs, two single cell configurations were tested with and without r-BMO7/BCY3 for comparison. The classic cathode material BCFZY was chosen due to its reliable and stable performance among various cathode materials [68]. The electrolyte thickness was controlled to approximately 20 μm, as shown in Fig. S11.

The IV-IP curves for both cells, operating in hydrogen and ammonia atmosphere at 550 °C, are shown in Fig. 3a. For the cell with the r-BMO7/BCY3 layer, the peak power densities (PPD) of the cell in hydrogen and ammonia are similar, suggesting that the ACL and anode effectively convert most of the ammonia into hydrogen and nitrogen. However, for the cell without an ACL, the performance difference in different atmospheres indicates that the ammonia decomposition efficiency of the bare anode is not satisfied. In addition to the PPD difference, the cell with r-BMO7/BCY3 ACL obtained a higher OCV, which suggests a higher hydrogen concentration than the cell without the ACL [69]. These results demonstrate that the ACL r-BMO7/BCY3 could enhance cell performance in both hydrogen and ammonia environments. The PPD of the cells in different atmospheres and temperatures can be seen in Fig. 3b, when using H₂ as fuel, the cell with r-BMO7/BCY3 ACL reached PPD of 716, 514, 335, 200, and 101 mW cm⁻² at 600, 550, 500, 450, and 400 °C, respectively. When ammonia was used as the fuel, the same cell reached a PPD of 680, 448, 273, 142, and 45 mW cm⁻² at corresponding temperatures. In contrast, the cell without an ACL achieved only 561 and 402 mW cm⁻² at 600 °C when operated with H₂ and NH₃, respectively. The detailed IV-IP result can be found in Fig. S12. Fig. S13 compares the PPD of the state-of-the-art DASOFC at 550 °C [32, 36,70]. The performance of the single cell with r-BMO7/BCY3 is comparable to the DASOFC at 550 °C.

To further assess the long-term stability, a stability test was conducted in an ammonia environment. As shown in Fig. 3c, the single cell

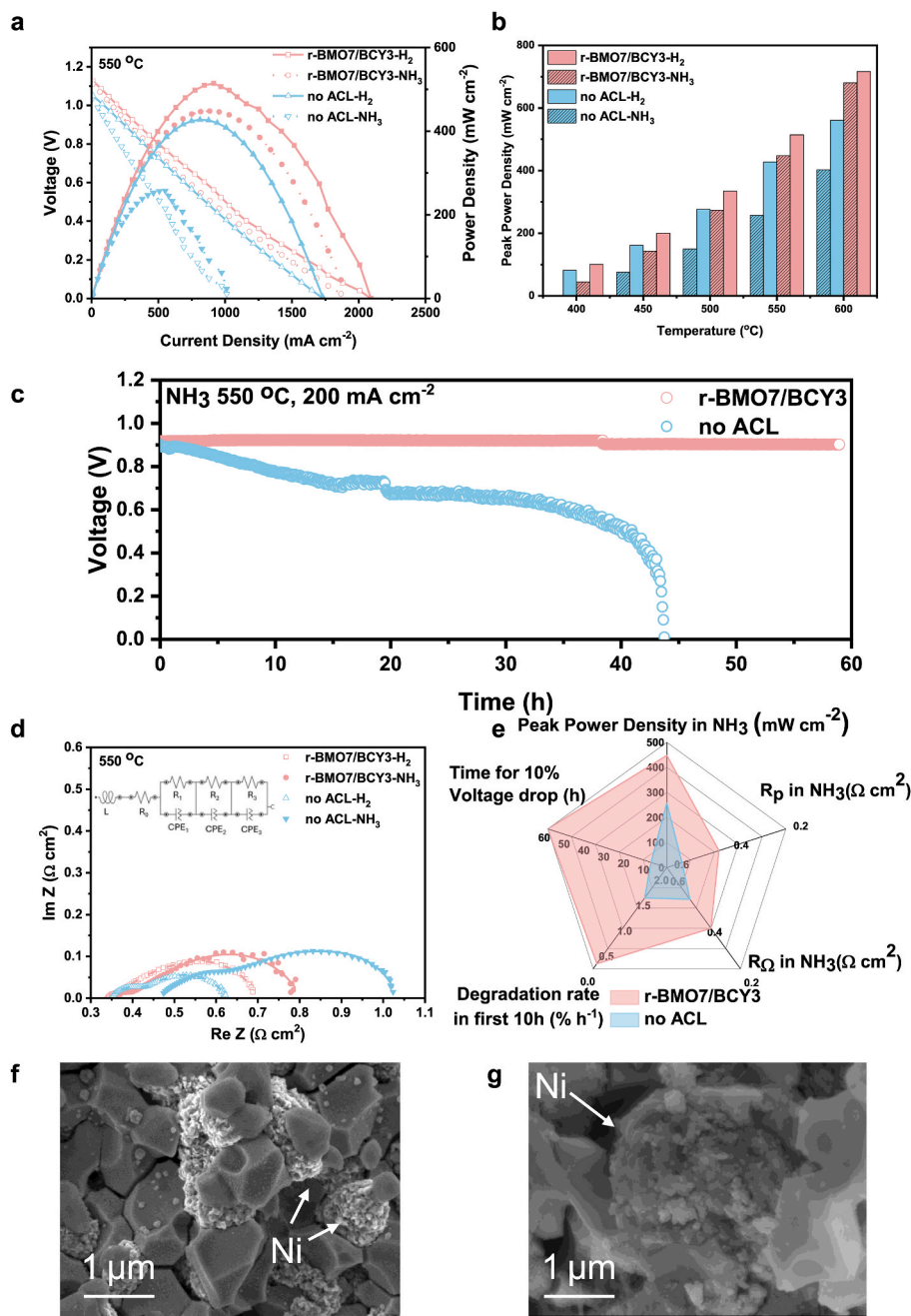


Fig. 3. (a) I–V and I–P curves of single cell with and without r-BMO7/BCY3 ACL in H₂ and NH₃ at 550 °C, (b) Comparison of the single cell performance with and without r-BMO7/BCY3 ACL in H₂ and NH₃ between 600 and 400 °C, (c) The stability of the fuel cells with r-BMO7/BCY3 ACL and without ACL operating in 200 mA cm⁻² under NH₃ condition at 550 °C, (d) Nyquist plots of single cell with and without r-BMO7/BCY3 ACL in H₂ and NH₃ at 550 °C, (e) Radar chart of cell with and without r-BMO7/BCY3 ACL for electrochemical performance (f) SEM figure of fuel cell with r-BMO7/BCY3 catalyst layer and (g) without catalyst layer after stability test at 550 °C.

without the ACL exhibits slow degradation, followed by a rapid performance drop and sudden failure after 43 h of operation at 200 mA cm⁻² under 550 °C in ammonia. In contrast, the cell with the r-BMO7/BCY3 ACL showed stable power output for nearly 60 h, with only minor fluctuations observed at 40 h due to a device restart. This demonstrates that the r-BMO7/BCY3 ACL helps prevent anode degradation and failure in ammonia environments.

The Nyquist plot of both cells in hydrogen and ammonia based on electrochemical impedance spectroscopy (EIS) analysis performed at 550 °C can be found in Fig. 3d. The EIS spectra were analysed based on LR₀(R₁/CPE₁)(R₂/CPE₂)(R₃/CPE₃) equivalent circuit. In the hydrogen atmosphere, both cells exhibited similar ohmic and polarisation

resistances, with the cell without an ACL even showing a lower polarisation resistance. However, in ammonia, the cell with r-BMO7/BCY3 displayed both lower ohmic and polarisation resistances compared to the cell without an ACL. This difference explains the higher power density observed for the cell with the ACL in ammonia. In addition to equivalent circuit analysis, Distribution of Relaxation Times (DRT) analysis was conducted to further investigate the electrode behavior of the cells operating in hydrogen and ammonia atmospheres, as shown in Fig. S14. In both atmospheres, a peak was observed at high frequencies (above 10⁴ Hz) for both cells. This peak is attributed to charge transfer and ionic conduction processes occurring at the anode [71]. When the atmosphere changes from hydrogen to ammonia, the cell without an

ACL shows a significant increase in resistance at mid to low frequencies. This increase is associated with gas diffusion limitations in the anode layer [72,73], where factors such as hydrogen concentration and diffusion pathways have an impact. In contrast, the cell with the r-BMO7/BCY3 ACL shows a smaller increase in resistance in this frequency range, indicating that the change in atmosphere has a less pronounced effect on its performance. This finding explains why the cell with the r-BMO7/BCY3 ACL achieves better performance at 550 °C. The EIS of the cells, in both atmospheres between 600 and 400 °C, can be found in Fig. S15. The similar ohmic resistance in both cells indicates that the electrolyte thickness is comparable. Given that both cells used BCFZY cathodes of similar thickness, the difference in polarisation resistance can be attributed to the anode reactions. For the cell with the ACL, lower polarisation resistance was observed in both hydrogen and ammonia atmosphere, particularly in ammonia.

Fig. 3e displays a radar chart summarising the electrochemical performance of the cells with and without r-BMO7/BCY3 ACL. The EIS results in ammonia show that the cells with r-BMO7/BCY3 ACL exhibit better electrochemical performance, as evidenced by their lower ohmic and polarisation resistances compared to the cell without an ACL. In addition to the EIS results, the degradation rate of the cell without an ACL was obvious compared to the cell with the r-BMO7/BCY3 layer. After 10h, the cell without an ACL completely failed around 43 h, while the cell with the r-BMO7/BCY3 ACL observers negligible reduction in performance for more than 60h. As a result, the cell with the r-BMO7/BCY3 ACL demonstrates superior performance compared to the cell without an ACL.

The single cells after the stability test in ammonia were examined by SEM, as shown in Fig. 3f and g. For the cell with the r-BMO7/BCY3 ACL, as shown in Fig. 3f, the Ni particles have an average diameter of 1 µm, with some nanosized particles present on the BZCYb anode support surface. The coarsening and agglomeration of Ni on the anode side were significantly reduced compared to the cell without an ACL, as shown in Fig. 3g. On the other hand, for the single cell without the ACL, the average diameter of the Ni particles was more than 2 µm, and the distribution of the Ni nanoparticles was less uniform, indicating significant agglomeration of Ni on the anode side. Compared to the Ni particles in the cell with the r-BMO7/BCY3 ACL, coarsening was observed in the cell without the ACL. This suggests Ni coarsened and agglomerated during the ammonia decomposition reaction, as the anode was exposed to high-concentration ammonia gas. This process led to changes and degradation in the Ni morphology, as well as damage to the Ni-BZCYb interface, which can ultimately cause the anode structure to break down and result in sudden cell failure, as observed by other researchers [17,35]. The r-BMO7/BCY3 ACL on the anode surface helps convert most of the ammonia into hydrogen and nitrogen, thereby lowering the ammonia partial pressure on the Ni surface and mitigating coarsening and agglomeration during cell operation.

4. Conclusion

In this study, a noble metal-free ACL strategy was applied to the PCFC anode to address the poor stability of Ni-based anodes under NH₃ conditions. The catalyst layer, composed of CFN alloy, enhances ammonia decomposition catalytic activity at reduced temperatures and mitigates the morphological degradation of Ni in the single cell. The formation of the CFN alloy in a reduced atmosphere enhances metal oxide phase separation and reduction to metal, ammonia adsorption, and nitrogen desorption, all of which contribute to improved ammonia decomposition efficiency. The BaO that comes from BMO increases the basicity of the catalyst, while the BCY support provides a proton conduction medium, both of which facilitate the ammonia decomposition process. As a result, the power density and lifetime of the single cell operating under ammonia conditions are significantly enhanced. The button cell with the r-BMO7/BCY3 ACL demonstrated stable performance for over 60 h with negligible performance loss. This noble metal-

free anode catalyst layer strategy offers a cost-effective approach to improving the long-term operation of PCFCs at reduced temperatures.

CRedit authorship contribution statement

Tianjiu Zhu: Writing – review & editing, Writing – original draft, Validation, Methodology, Investigation, Formal analysis, Data curation, Conceptualization. **Desheng Feng:** Methodology, Investigation, Formal analysis, Data curation. **Zhixin Luo:** Writing – original draft, Formal analysis, Data curation. **Zehua Wang:** Formal analysis, Data curation. **Beibei Ma:** Formal analysis, Data curation. **Zongping Shao:** Writing – review & editing, Writing – original draft, Visualization, Validation, Supervision, Resources, Project administration, Methodology, Investigation, Conceptualization. **Zhonghua Zhu:** Writing – review & editing, Writing – original draft, Visualization, Validation, Supervision, Software, Resources, Project administration, Methodology, Investigation, Funding acquisition, Conceptualization. **Lei Ge:** Writing – review & editing, Writing – original draft, Supervision, Resources, Project administration, Methodology, Investigation, Funding acquisition, Formal analysis, Conceptualization.

Declaration of competing interest

The authors declare that they have no known competing financial interests or personal relationships that could have appeared to influence the work reported in this paper.

Acknowledgments

The authors acknowledge the facilities, and the scientific and technical assistance, of the Australian Microscopy & Microanalysis Research Facility at the Centre for Microscopy and Microanalysis, The University of Queensland. This research was undertaken on the PD (PDR22674, PDR23596) beamline at the Australian Synchrotron, part of ANSTO. This work is financially supported by the Australian Research Council (ARC) DP200101397, DP250102334 and FT220100166.

Appendix A. Supplementary data

Supplementary data to this article can be found online at <https://doi.org/10.1016/j.ijhydene.2025.04.461>.

References

- [1] Duan C, et al. Readily processed protonic ceramic fuel cells with high performance at low temperatures. *Science* 2015;349(6254):1321–6.
- [2] Yang L, et al. Enhanced sulfur and coking Tolerance of a mixed ion conductor for SOFCs: BaZr_{0.1}Ce_{0.7}Y_{0.2-x}Yb_xO_{3-δ}. *Science* 2009;326(5949):126–9.
- [3] Liang M, et al. A new durable surface nanoparticles-modified perovskite cathode for protonic ceramic fuel cells from selective cation exsolution under oxidizing atmosphere. *Adv Mater* 2022;34(10):2106379.
- [4] Feng D, et al. In situ formation of a melt-solid interface toward stable oxygen reduction in protonic ceramic fuel cells. *Adv Funct Mater* 2025;35(12):2417425.
- [5] Wang Z, et al. New understanding and improvement in sintering behavior of cerium-rich perovskite-type protonic electrolytes. *Adv Funct Mater* 2024;34(38):2402716.
- [6] Zhao Y, et al. An efficient direct ammonia fuel cell for affordable carbon-neutral transportation. *Joule* 2019;3(10):2472–84.
- [7] Feng J, et al. Applications of rare earth oxides in catalytic ammonia synthesis and decomposition. *Catal Sci Technol* 2021;11(19):6330–43.
- [8] Rivard E, Trudeau M, Zaghbi K. Hydrogen storage for mobility: a review. *Materials* 2019;12. <https://doi.org/10.3390/ma12121973>.
- [9] Lee JE, et al. Catalytic ammonia decomposition to produce hydrogen: a mini-review. *Chem Eng J* 2023;475:146108.
- [10] Valera-Medina A, et al. Ammonia for power. *Prog Energy Combust Sci* 2018;69:63–102.
- [11] Duan C, et al. Highly durable, coking and sulfur tolerant, fuel-flexible protonic ceramic fuel cells. *Nature* 2018;557(7704):217–22.
- [12] Liu F, et al. Redesigning protonic ceramic electrochemical cells to lower the operating temperature. *Sci Adv* 2025;11(2):eadq2507.
- [13] Xie Z, et al. Nanostructured fuel electrodes for low-temperature proton- and oxygen-ion-conducting solid oxide cells. *J Energy Chem* 2025;106:302–30.

- [14] Yan J, et al. Nanotechnology-based design and fabrication of advanced electrolytes for solid oxide cells. *Small* n/a(n/a):2409648. <https://doi.org/10.1002/sml.202409648>.
- [15] Shi H, et al. Advances in power generation from ammonia via electrocatalytic oxidation in direct ammonia fuel cells. *Chem Eng J* 2024;488:150896.
- [16] Rathore SS, et al. Direct ammonia solid-oxide fuel cells: a review of progress and prospects. *Int J Hydrogen Energy* 2021;46(71):35365–84.
- [17] Feng D, et al. K and Mg Co-doped perovskite oxide for enhanced anode of direct ammonia protonic ceramic fuel cell. *Int J Hydrogen Energy* 2024;88:272–8.
- [18] Huang Z, et al. Highly active internal catalyst promoting the efficient ammonia decomposition and durability of protonic ceramic fuel cells. *Ceram Int* 2024;50(7, Part A):10551–9.
- [19] Pan Y, et al. A high-performance and durable direct NH₃ tubular protonic ceramic fuel cell integrated with an internal catalyst layer. *Appl Catal B Environ* 2022;306:121071.
- [20] Baiker A, Maciejewski M. *Formation and thermal stability of copper and nickel nitrides*. Journal of the Chemical Society, Faraday Transactions 1. Physical Chemistry in Condensed Phases 1984;80(8):2331–41.
- [21] Batool SY, et al. Leveraging Ni ex-solved perovskite structure to design a ternary-phase-catalyzed composite anode for high-performance direct ammonia solid oxide fuel cells. *ACS Appl Energy Mater* 2025;8(4):2452–64.
- [22] Yang J, et al. A stability study of Ni/Yttria-Stabilized zirconia anode for direct ammonia solid oxide fuel cells. *ACS Appl Mater Interfaces* 2015;7(51):28701–7.
- [23] Sun S, et al. Ammonia as hydrogen carrier: advances in ammonia decomposition catalysts for promising hydrogen production. *Renew Sustain Energy Rev* 2022;169:112918.
- [24] Zhu L, et al. Ammonia-fed reversible protonic ceramic fuel cells with Ru-based catalyst. *Commun Chem* 2021;4(1):121.
- [25] Jeong HJ, et al. High-performance ammonia protonic ceramic fuel cells using a Pd inter-catalyst. *Small* 2023;19(22):2208149.
- [26] He F, et al. Self-construction of efficient interfaces ensures high-performance direct ammonia protonic ceramic fuel cells. *Adv Mater* 2023;35(42):2304957.
- [27] Chen L, et al. An active and durable ammonia cracking layer for direct ammonia protonic ceramic fuel cells. *Materials Today Catalysis* 2024;7:100072.
- [28] Ganley JC, et al. A priori catalytic activity correlations: the difficult case of hydrogen production from ammonia. *Catal Lett* 2004;96(3):117–22.
- [29] Dang H, Song L, Shi G. Efficient ammonia conversion in proton conducting fuel cells: combined application of dendritic anodes and nanofiber catalysts. *Int J Hydrogen Energy* 2024;85:715–25.
- [30] Wang L, et al. Halloysite-nanotube-supported Ru nanoparticles for ammonia catalytic decomposition to produce CO_x-free hydrogen. *Energy & Fuels* 2011;25(8):3408–16.
- [31] Zhang H, et al. An efficient and durable anode for ammonia protonic ceramic fuel cells. *Energy Environ Sci* 2022;15(1):287–95.
- [32] Lan H, et al. Effect of increasing Fe catalytic decomposition layer of ammonia on the performance and stability of ammonia electrode. *J Power Sources* 2024;593:233987.
- [33] Zheng K, et al. An experimental study of ammonia decomposition rates over cheap metal catalysts for solid oxide fuel cell anode. *Int J Hydrogen Energy* 2023;48(50):19188–95.
- [34] Liang M, et al. In situ exsolved CoFeRu alloy decorated perovskite as an anode catalyst layer for high-performance direct-ammonia protonic ceramic fuel cells. *Adv Funct Mater* 2024;34(48):2408756.
- [35] Zhang H, et al. In situ formed catalysts for active, durable, and thermally stable ammonia protonic ceramic fuel cells at 550 °C. *Energy Environ Sci* 2024;17(10):3433–42.
- [36] Liu Z, et al. Boosting ammonia-fueled protonic ceramic fuel cells with RuFe nanoparticle exsolution: enhanced performance via secondary redox treatment. *Adv Funct Mater* 2025;35(15):2420214.
- [37] Song Y, et al. Infiltrated NiCo alloy nanoparticle decorated perovskite oxide: a highly active, stable, and antisintering anode for direct-ammonia solid oxide fuel cells. *Small* 2020;16(28):2001859.
- [38] Chen T-B, et al. Enhancing the ammonia catalytic decomposition of lanthanum strontium titanate nickel perovskite catalysts via a balanced cation doping and deficiency strategy. *Energy & Fuels* 2024;38(6):5449–56.
- [39] Cavazzani J, et al. Exsolution in Ni-doped lanthanum strontium titanate: a perovskite-based material for anode application in ammonia-fed Solid Oxide Fuel Cell. *Int J Hydrogen Energy* 2022;47(29):13921–32.
- [40] Kim H, et al. Exsolution of Ru nanoparticles on BaCe_{0.9}Y_{0.1}O_{3-δ} modifying geometry and electronic structure of Ru for ammonia synthesis reaction under mild conditions. *Small* 2023;19(6):2205424.
- [41] Rioja-Monllor L, et al. Processing of high performance composite cathodes for protonic ceramic fuel cells by exsolution. *J Mater Chem A* 2019;7(14):8609–19.
- [42] Okura K, et al. Ammonia decomposition over Ni catalysts supported on perovskite-type oxides for the on-site generation of hydrogen. *RSC Adv* 2018;8(56):32102–10.
- [43] Miyazaki K, et al. Development of Ni–Ba(Zr,Y)O₃ cermet anodes for direct ammonia-fueled solid oxide fuel cells. *J Power Sources* 2017;365:148–54.
- [44] Miyazaki K, et al. Impact of the ammonia decomposition reaction over an anode on direct ammonia-fueled protonic ceramic fuel cells. *Sustain Energy Fuels* 2020;4(10):5238–46.
- [45] Toby BH, Von Dreele RB. GSAS-II: the genesis of a modern open-source all purpose crystallography software package. *J Appl Crystallogr* 2013;46(2):544–9.
- [46] Cline JP, et al. The certification of SRM 640c; the primary NIST line position SRM for powder diffraction4. Australia: Australian X-ray Analytical Association; 1999. p. 210.
- [47] Black D, et al. Certification of standard reference material 660b. 2011.
- [48] Kabekkodu SN, Dosen A, Blanton TN. PDF-5+ : a comprehensive Powder Diffraction File™ for materials characterization. *Powder Diffr* 2024;39(2):47–59.
- [49] Fairley N, et al. Systematic and collaborative approach to problem solving using X-ray photoelectron spectroscopy. *Appl Surf Sci Adv* 2021;5:100112.
- [50] Song Y, et al. Self-assembled triple-conducting nanocomposite as a superior protonic ceramic fuel cell cathode. *Joule* 2019;3(11):2842–53.
- [51] Luo K, et al. In situ self-assembly of a high active and durable composite electrode for protonic ceramic fuel cells. *Ceram Int* 2024;50(20, Part C):40586–93.
- [52] Zou D, et al. The BaCe_{0.16}Y_{0.04}Fe_{0.80}O_{3-δ} nanocomposite: a new high-performance cobalt-free triple-conducting cathode for protonic ceramic fuel cells operating at reduced temperatures. *J Mater Chem A* 2022;10(10):5381–90.
- [53] Wu J., et al. A new nanocomposite electrode developed from environmental atmosphere triggered reconstruction for efficient reversible protonic ceramic cells. *Adv Energy Mater* n/a(n/a):2404118. <https://doi.org/10.1002/aenm.202404118>.
- [54] Cao P, et al. Atomic-Scale insights into nickel exsolution on LaNiO₃ catalysts via in situ electron microscopy. *J Phys Chem C* 2022;126(1):786–96.
- [55] Lin K-H, Wang C-B, Chien S-H. Catalytic performance of steam reforming of ethanol at low temperature over LaNiO₃ perovskite. *Int J Hydrogen Energy* 2013;38(8):3226–32.
- [56] Wang Y, et al. Microscopic insight into ruthenium exsolution from LaFe_{0.9}Ru_{0.1}O₃ perovskite. *Chem Mater* 2024;36(12):6246–56.
- [57] Lee JG, et al. Synthesis and application of hexagonal perovskite BaNiO₃ with quadrivalent nickel under atmospheric and low-temperature conditions. *Chem Commun* 2016;52(71):10731–4.
- [58] Siebert E, et al. Electrochemical and Raman study of La_{0.7}Sr_{0.3}Co_{0.8}Fe_{0.2}O_{3-δ} reduction. *Solid State Ionics* 2013;247–248:30–40.
- [59] Biesinger MC, et al. Resolving surface chemical states in XPS analysis of first row transition metals, oxides and hydroxides: Cr, Mn, Fe, Co and Ni. *Appl Surf Sci* 2011;257(7):2717–30.
- [60] Kim YH, et al. Nanoparticle exsolution on perovskite oxides: insights into mechanism, characteristics and novel strategies. *Nano-Micro Lett* 2023;16(1):33.
- [61] Tsekouras G, Neagu D, Irvine JTS. Step-change in high temperature steam electrolysis performance of perovskite oxide cathodes with exsolution of B-site dopants. *Energy Environ Sci* 2013;6(1):256–66.
- [62] Neagu D, et al. In situ growth of nanoparticles through control of non-stoichiometry. *Nat Chem* 2013;5(11):916–23.
- [63] Wang Y, et al. One-step synthesis of Ni/yttrium-doped barium zirconates catalyst for on-site hydrogen production from NH₃ decomposition. *Int J Hydrogen Energy* 2022;47(4):2608–21.
- [64] Xie P, et al. Highly efficient decomposition of ammonia using high-entropy alloy catalysts. *Nat Commun* 2019;10(1):4011.
- [65] Jia W, et al. Facilitated ammonia decomposition and enhanced hydrogen diffusion in 10Ni-Ce_{0.8}Zr_{0.2}O₂ as anode catalytic functional layer for low-temperature direct ammonia fuel cells. *Chem Eng J* 2025;504:158976.
- [66] Okura K, et al. Promotion effect of rare-earth elements on the catalytic decomposition of ammonia over Ni/Al₂O₃ catalyst. *Appl Catal Gen* 2015;505:77–85.
- [67] Long RQ, Yang RT. Temperature-programmed desorption/surface reaction (TPD/TPSR) study of Fe-exchanged ZSM-5 for selective catalytic reduction of nitric oxide by ammonia. *J Catal* 2001;198(1):20–8.
- [68] Luo Z, et al. First observation of electrode-correlated protonic conductivity of perovskite-type electrolytes and way towards optimization. *Energy Environ Sci* 2024;17(12):4115–25.
- [69] Luo Z, et al. Performance deviation analysis and reliability improvement during experimental development of lab-scale solid oxide single cells. *Energy Environ Sci* 2024;17(19):6873–96.
- [70] He F, et al. A new Pd doped proton conducting perovskite oxide with multiple functionalities for efficient and stable power generation from ammonia at reduced temperatures. *Adv Energy Mater* 2021;11(19):2003916.
- [71] Sumi H, et al. Degradation evaluation by distribution of relaxation times analysis for microtubular solid oxide fuel cells. *Electrochim Acta* 2020;339:135913.
- [72] Dierickx S, Weber A, Ivers-Tiffée E. How the distribution of relaxation times enhances complex equivalent circuit models for fuel cells. *Electrochim Acta* 2020;355:136764.
- [73] Ya Y, et al. Effect of operating temperature on ammonia decomposition behavior and cell performance of direct ammonia solid oxide fuel cells. *Int J Hydrogen Energy* 2024;91:659–72.